Article

Product Yields Dependency on the Carbide Phase Presence in Cobalt and Iron SBA-15 Catalysts Structure in the Fischer–Tropsch Synthesis

Nikita Sharkov [1], Zahra Gholami [1,*], Ivana Hradecká [1,2], Zdeněk Tišler [1] and Josef Šimek [1]

[1] ORLEN UniCRE, a.s., Revoluční 1521/84, 400 01 Ústí nad Labem, Czech Republic; nikita.sharkov@orlenunicre.cz (N.S.); ivana.hradecka@orlenunicre.cz (I.H.); zdenek.tisler@orlenunicre.cz (Z.T.); josef.simek@unipetrol.cz (J.Š.)

[2] Department of Chemistry, Faculty of Agrobiology, Food and Natural Resources, Czech University of Life Sciences Prague, Kamýcká 129, 165 00 Prague, Czech Republic

* Correspondence: zahra.gholami@orlenunicre.cz; Tel.: +420-731-576-893

Abstract: The use of carbide catalysts in Fischer–Tropsch synthesis (FTS) is an active area of research, as carbide phases have been shown to improve the stability and performance of catalysts in this reaction. This study compared the catalytic activity and product selectivity of cobalt and iron catalysts supported on SBA-15, with and without a carbide phase and reduction treatment before the reaction. Results showed that the presence of the carbide phase had a noticeable influence on the catalytic behavior of the catalysts, and the reduction of the catalyst with hydrogen also affected the product selectivity. The presence of the carbide phase in non-reduced cobalt catalysts resulted in increased selectivity to liquid phase products, as evidenced by a CO conversion of 37% with 68% selectivity to the products in the liquid phase. The catalytic activity of the iron carbide catalyst for CO dissociation was found to be 38% after reducing the catalyst with hydrogen, leading to the formation of more active sites. The presence of metal carbides and formation of metallic cobalt and iron during the FT reaction and reduction step was found to have a significant effect on the catalytic performance and product selectivity. The findings of this research provide new insights into the role of carbide in the performance of cobalt and iron catalysts in Fischer–Tropsch synthesis.

Keywords: Fischer–Tropsch synthesis; carbide catalyst; CoCx/SBA-15; FeCx/SBA-15

1. Introduction

Nowadays, the Fischer–Tropsch synthesis (FTS) is beginning to receive more attention as an alternative route to fuels and valuable chemicals. Since the technological progress in FTS has led to the possibility of converting synthesis gas (syngas) derived from biomass processing, in addition to coal, into liquid fuels, this makes the process even more important for the environment. Nevertheless, the production of hydrocarbons from syngas is a complex catalytic process that includes a large number of sequential and parallel transformations, where the composition of the products is determined by the nature of the catalyst, which is mainly a VIII group transition metal (Co, Fe, Ni, and Ru) [1].

Catalysts play a crucial role in Fischer–Tropsch synthesis (FTS), where the conversion of feedstocks to fuels and chemicals takes place. In this regard, one of the main tasks is the design of a catalyst with not only high activity and stability, but also high selectivity with respect to the formation of a certain range of hydrocarbon products. Ruthenium is the most active FT catalyst, but its high price and limited world reserves preclude industrial applications. In the case of nickel, at elevated temperatures, the selectivity changes mainly to methane [2], which is an undesirable product since FT process conditions are usually optimized to produce more valuable, higher molecular weight liquid fuels, which are more valuable products. When the feedstock is natural gas with a high H to C ratio,

cobalt catalysts exhibit better activity for FTS compared to iron-based catalysts, making water–gas shift reactions (WGSR) unnecessary for these metal catalysts. On the other hand, catalysts containing iron with enhanced activity for the water–gas shift reaction (WGSR) are desirable for converting low-quality feedstocks, such as coal or biomass, into syngas. This is important because syngas from such feedstocks typically contains low hydrogen, necessitating a water–gas shift reaction to increase the hydrogen content. Iron catalysts tend to form several phases, including oxides and carbides, during the reaction. The regulation of these phase transformations plays a critical role in sustaining catalytic activity and preventing degradation of the catalyst particles [3].

To maximize the yield of the FTS product, it is crucial to identify the active phase(s) of the catalyst under the reaction conditions. FT catalysts are commonly composed of metal oxide nanoparticles, such as Co_3O_4 for cobalt and Fe_2O_3 for iron, prior to the reaction. The catalyst can be activated by treatment with H_2 or CO/synthesis gas for iron to convert it into its active form. During FTS, metallic and oxide species are commonly observed to coexist after activation. For iron, the carbide particles are considered to be the active phase, while for cobalt, its metallic form [4]. However, from 2011 to the present, numerous studies have reported cobalt carbide as a highly active phase in cobalt-based FT reaction to olefins [5–8] or oxygenates [9–13]. These studies showed that cobalt carbide was stabilized by an oxide compound and/or an alkaline promoter [14].

Additionally, the choice of catalyst support strongly affects the catalytic activity, as the physicochemical properties of the support impact the metal-support interaction, metal dispersion, crystallite size, and mass transfer of reactants and products. The surface properties, pore volume, and pore size play a significant role in determining selectivity and catalytic activity. The most commonly used supports are zeolites, alumina, silica, titanium dioxide, and carbides [15]. Among others, the SBA series is a mesoporous silica widely recognized for its remarkable stability under both thermal and hydrothermal conditions [16], as well as its high surface area and pore volume [17]. In addition, its porosity can be easily controlled [18], making it a popular choice as catalyst support. SBA-15, in particular, has been extensively studied due to its high thermal stability, uniform pore size, and hexagonal arrangement of one-dimensional cylindrical channels, making it an excellent support material for catalysts [19].

The novelty of this work lies in the investigation of the catalytic properties of SBA-15-supported cobalt and iron catalysts modified with a carbide phase for the Fischer–Tropsch synthesis. While cobalt and iron catalysts are commonly used in this process, the addition of a carbide phase has been shown to enhance the activity and selectivity of cobalt-based FT reactions. In this study, we aimed to compare the catalytic activity and product selectivity of the cobalt and iron catalysts with and without a carbide phase, with a particular focus on the role of the carbide phase in the catalyst behavior. Our findings will contribute to the development of more efficient and selective catalysts for the production of valuable liquid fuels and chemicals from syngas, especially from biomass processing, thus addressing a pressing environmental concern.

2. Experimental

2.1. Support Preparation

The mesoporous material, SBA-15, utilized for catalyst support, was synthesized following the protocol described by Zukal et al. [20]. The support materials included amphiphilic triblock copolymer Pluronic® P123 (P123, Sigma-Aldrich, Schnelldorf, Germany) and silica, added through tetraethyl orthosilicate (TEOS, Sigma-Aldrich, Schnelldorf, Germany). The reaction mixture was prepared with a molar ratio of 1 TEOS:0.017 P123:6.1 HCl:197 H_2O and maintained at 35 °C for 24 h, followed by 66 h at 95 °C under static conditions. The product was then filtered, washed with distilled water, and dried overnight at 80 °C. The final step involved calcination in air at a temperature of 540 °C for 8 h, with a temperature ramp of 1 °C/min.

2.2. Catalyst Preparation

The Co/SBA-15 and Fe/SBA-15 catalysts were synthesized using the incipient wetness impregnation (IWI) technique. The method involved dissolving the required number of precursors, cobalt nitrate hexahydrate (Lech-Ner s.r.o., p.a. purity), or iron nitrate nonahydrate (Lech-Ner s.r.o., p.a. purity) in deionized water at room temperature. The resultant solution was then added to the SBA-15 support powder. The impregnated catalysts were dried sequentially overnight at 120 °C and 250 °C.

The CoCx/SBA-15 and FeCx/SBA-15 carbide catalysts were prepared by exposing 4 g of the precursor to a gas mixture containing 20% CH_4 in H_2 with a flow rate of 300 cm^3/min at a temperature of 300 °C for 3 h according to a method previously described in our work [21]. After carbidation, the catalysts were purged with N_2 for 30 min and then passivated for 2 h under 1% O_2 in Ar with a flow rate of 75 cm^3/min (Figure 1).
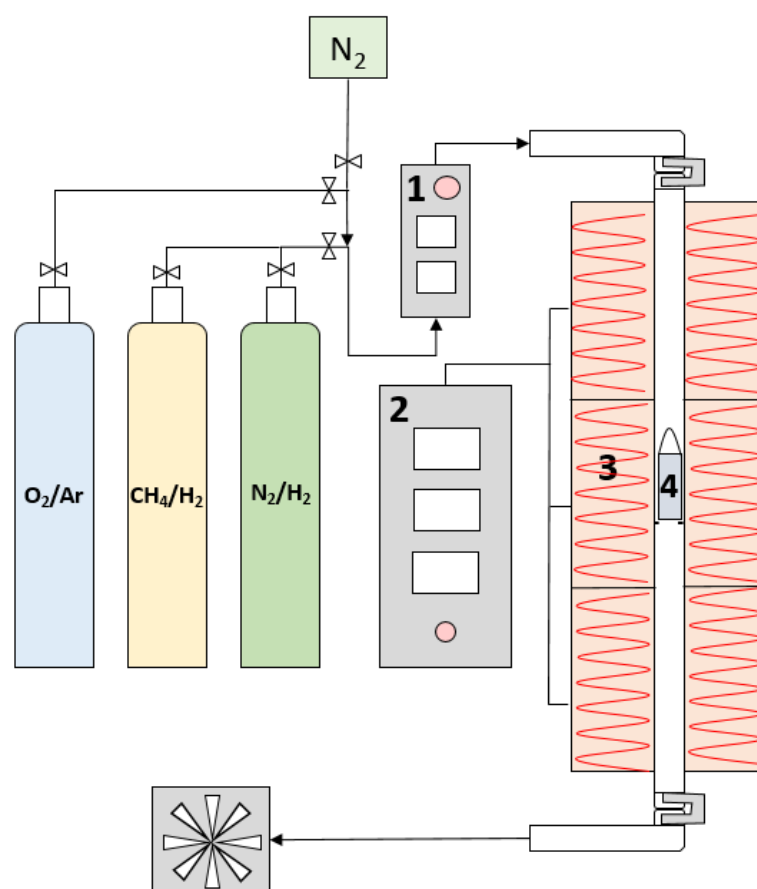
Figure 1. The R41 reactor scheme for the synthesis of catalysts (1—gas flow regulator, 2—temperature regulator, 3—furnace (3 zones), 4—quartz glass cuvette with sample).

2.3. Catalysts Characterization

Synthesized catalysts were characterized using scanning electron microscopy (SEM), N_2 adsorption–desorption, X-ray diffraction (XRD) analysis, thermogravimetric analysis (TGA), inductively coupled plasma (ICP) analysis, and H_2-temperature programmed reduction (H_2-TPR).

2.3.1. SEM

The morphology of the samples was examined using a HITACHI scanning electron microscope (Chiyoda, Tokyo, Japan) S-4800 FEG equipped with secondary and backscattered electron detectors. To verify the presence of carbon in the fresh carbide catalysts, energy-dispersive X-ray spectroscopy (EDX) was utilized. EDX was conducted at a voltage of 15 kV and a working distance of 15 mm. Compositional analysis was also conducted

using EDX under the same voltage and working distance. Compositional mapping was performed at the same working distance and voltage.

2.3.2. Nitrogen Adsorption–Desorption

To analyze the surface properties of the catalyst samples, a N_2 physisorption isotherm was obtained using an Autosorb iQ instrument (Quantachrome Instruments, Boynton Beach, FL, USA) at its normal boiling point of -196 °C. Prior to the analysis, the samples were evacuated at 110 °C for 16 h. The Brunauer–Emmett–Teller (BET) and Barrett–Joyner–Halenda (BJH) equations were utilized to determine the catalyst's surface area, pore size, and pore volume.

2.3.3. XRD

Powder X-ray diffraction (XRD) analysis was performed using a D8 Advance Eco X-ray diffractometer (Bruker AXS GmbH, Karlsruhe, Germany) equipped with an X-ray lamp with Cu anode ($\lambda = 1.5406$ Å). Samples were homogenized manually in an agate mortar, triturated with isopropanol, and applied to a monocrystalline (Si). Following that, samples were measured in the range from 5° to 70° (2Theta) with 0.04° resolution and an integration time of 1 s. The diffraction patterns were analyzed using Diffrac. Eva V4.1.1 software, and the identification of crystalline phases was performed with the ICDD PDF4+ database of diffraction data.

2.3.4. TGA

Short thermogravimetric tests were carried out on TGA Discovery Series from TA Instruments for all fresh catalysts using one temperature ramp up to 900 °C at a heating rate of 10 °C/min in nitrogen and oxygen gases.

2.3.5. TGA Long-Term Analyses

TGA tests were performed for fresh non-carbide catalysts using a Linseis equipment model PT 1600 to monitor the formation of carbides on the catalyst surface. Before each analysis, samples were pressed into pellets using a manual powder tablet compression machine (443 MPa). The temperature program included four temperature ramps up to 800 °C with a heating rate of 5 °C/min using different gases: air, hydrogen, and methane, and each ramp was followed by a cooling step in inert nitrogen gas to 40 °C.

2.3.6. ICP-OES

Inductively coupled plasma optical emission spectrometry (ICP-OES) was performed to determine the percentage of carbon and other elements in the catalysts using an Agilent 725 spectrometer with a cross-dispersed echelle scheme and a CCD photon detector. Solid catalyst samples were measured after wet decomposition with acids.

2.3.7. H_2-TPR

To examine the reducibility of the samples, the temperature-programmed reduction method was used to characterize the fresh catalysts. A sample weight of approximately 100 mg was used in the analysis, and the Autochem 2950 HP instrument (Micromeritics Instrument Corporation, Norcross, GA, USA) was employed. Prior to analysis, the sample was pretreated in Ar up to 400 °C using a temperature ramp of 10 °C/min. The TPR experiments were performed by applying a mixture of 10 vol.% H2 and 90 vol.% Ar at a flow rate of 50 mL/min and a linear temperature ramp of 10 °C/min up to 800 °C to obtain the H_2-TPR curve from the TCD detector.

2.4. Experimental Reaction Setup

The Fischer–Tropsch (FT) reaction was conducted in a 1 L autoclave reactor made of stainless steel from Parr instruments. To begin each test, 1.5 g of the catalyst and 35 mL of solvent (cyclohexane) were placed inside the reactor. The reactor was then

tightly sealed, and the temperature was gradually increased at a rate of 3 °C/min until it reached 230 °C under a pressure of 5 MPa of synthesis gas with a H_2/CO ratio of 2. The reaction was conducted for 6 h in batch mode with constant stirring at 800 rpm to prevent diffusion control effects. The conversion rate was calculated based on the pressure drop and the gas composition before and after the reaction. To investigate the effect of in situ catalyst reduction on the FT reaction, the reactor was heated to 300 °C at a rate of 3 °C/min, and then the H_2 pressure was increased to 5 MPa over a period of 5 h. After the reduction step, the reactor system was cooled to room temperature, the reaction gas was changed to syngas, and the FT reaction was conducted for 6 h at 230 °C and 5 MPa. Various chromatographic techniques were used to analyze the liquid and gaseous products of the FT reaction. The gaseous products were analyzed using an Agilent 7890A gas chromatograph equipped with three parallel channels that simultaneously collected data. Two channels had thermal conductivity detectors (TCD) for CO, H_2, N_2, and CO_2, and the third channel had a flame ionization detector (FID) for hydrocarbon detection. Liquid product samples were analyzed using Thermo Scientific ITQ Series GC/MS Ion Trap Mass Spectrometers.

3. Results and Discussion

3.1. Characterization of Catalysts

3.1.1. SEM

Figure 2 shows SEM images of the fresh carbide CoCx/SBA-15 and FeCx/SBA-15 catalysts. The dispersion of detected atoms is observable, and mapping distinguishes carbon atoms at 0.5 μm. Cobalt and iron were highly dispersed on the catalyst surface, with oxygen atoms also dispersed, and the pattern partially coincides with the image of silicon. Thus, it can be assumed that the visible oxygen is most likely located in the silica lattice. SEM images from the catalyst surfaces showed similar morphology, and EDX analysis confirmed that carbon atoms were introduced into the catalyst structure. Since graphitic carbon peaks were not observed in the XRD pattern of fresh carbide catalysts, the observed carbon in mapping analysis could be attributed to carbon species in carbide form. Silicon atoms forming the SBA-15 support were also clearly detected for both fresh CoCx/SBA-15 and FeCx/SBA-15 catalysts.
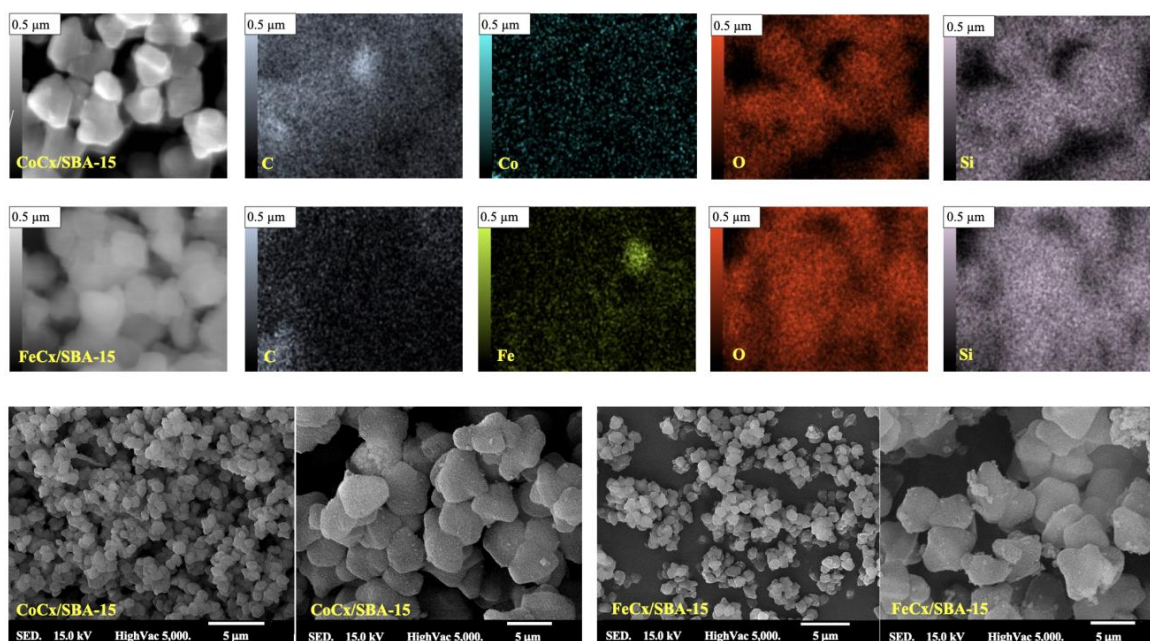
Figure 2. SEM images of the surface texture of CoCx/SBA-15 and FeCx/SBA-15 catalysts, including elemental mapping of C: carbon, Co: cobalt, Fe: iron, O: oxygen, and Si: silicon atoms obtained by EDX analysis with 0.5 μm resolution.

3.1.2. Nitrogen Adsorption–Desorption

Table 1 shows the specific surface area (SSA) and total pore volume of the fresh and used catalysts with and without carbide phase. The surface area of SBA-15 (842 m^2/g) decreased to 624 m^2/g and 649 m^2/g after loading 5 wt.% of cobalt and iron, respectively. The carbidation of the catalysts and the formation of CoCx and FeCx phase on the catalyst surface slightly increased the surface area of the carbided catalysts to 665 m^2/g and 679 m^2/g for CoCx/SBA-15 and FeCx/SBA-15, respectively. These results indicate that the presence of carbide phases in the catalyst structure can lead to an increase in the specific surface area. The total pore volume of the catalysts followed the same trend, where metal loading resulted in a lower pore volume due to pore blocking by metals, while carbidation and the formation of metal carbides resulted in a slightly higher pore volume.

Table 1. Surface area and total pore volume of fresh catalysts.

| Catalyst	BET Surface Area (m^2/g)	Total Pore Volume (cm^3/g)
SBA-15	842	1.23
Co/SBA-15	624	0.93
Fe/SBA-15	649	0.91
CoCx/SBA-15	665	1.05
FeCx/SBA-15	679	1.05

The adsorption–desorption isotherms of the fresh cobalt- and iron-based catalysts are shown in Figure 3a,b. The nitrogen adsorption isotherms of the catalysts (with and without carbide phase) exhibited a type IV isotherm, with a H_2 hysteresis loop for the SBA-15 supported catalysts. A defining characteristic of the isotherm observed for these materials is the presence of a hysteresis loop, which is related to capillary condensation taking place within the mesopores, resulting in limited uptake over a range of high P/P_0. The first portion of the type IV isotherm is attributed to monolayer to multilayer adsorption. Type IV isotherms are commonly observed for many mesoporous materials. The observed H2 hysteresis loop is attributed to the complex pore structure of the materials, which is characterized by ink-bottle-shaped pores with poor connectivity and an uneven pore structure [22,23]. The BJH technique was employed to determine the pore size of the catalysts. The pore sizes of both Co- and Fe-based catalysts (with and without carbide phase) were observed to be in the mesoporous range of 3–10 nm. Similar to the pore volume, the pore size of the catalysts slightly decreased after loading 5% cobalt or iron on SBA-15, which could be due to partial pore blockage. However, after carbidation of these Co/SBA-15 and Fe/SBA-15 catalysts, the pore sizes were almost similar to those of fresh SBA-15. These findings confirm that carbidation of the catalysts and formation of CoCx or FeCx on the surface resulted in a slight increase in the BET surface area, pore size, and pore volume of the catalysts.

Furthermore, in addition to the enhancement of surface properties, the catalytic activity and selectivity of the catalysts in the FTS can be influenced by the presence of carbide phases. The metal carbide phases can serve as active sites, facilitating the adsorption and activation of the reactants (CO and hydrogen), which are crucial to the FTS process. The presence of the metal carbide phases may also affect the distribution and stability of the active sites in the catalyst structure, which can influence the selectivity of the reaction towards different products.

3.1.3. XRD

The fresh and used cobalt- and iron-based catalysts were characterized to identify the cobalt- and iron-based phases in these catalysts (Figure 4a,b). The strong and broad peak at 2theta 15–30° is attributed to the amorphous structure of the SBA-15 [24,25]. Peaks belonging to the cubic phase Co_3O_4 (PDF card no. 65-3103) at 2theta of 19°, 31.4°, 37°, 45°, 55.9°, 59.5°, and 65.4° were observed in the fresh Co/SBA-15 catalyst. After

using this catalyst in the FT reaction without reduction, the catalyst exposed to syngas for 6 h (U-Co/SBA-15-WR) showed new peaks belonging to cobalt with a hexagonal closed-packed (hcp) structure (PDF card no. 00-005-0727) at 47.5°, and a face-centered cubic structure (fcc) of cobalt (PDF card no. 00-001-1259) at 44.4°, resulting from the reduction of the catalyst by exposing it to $H_2 + CO$ during the reaction.
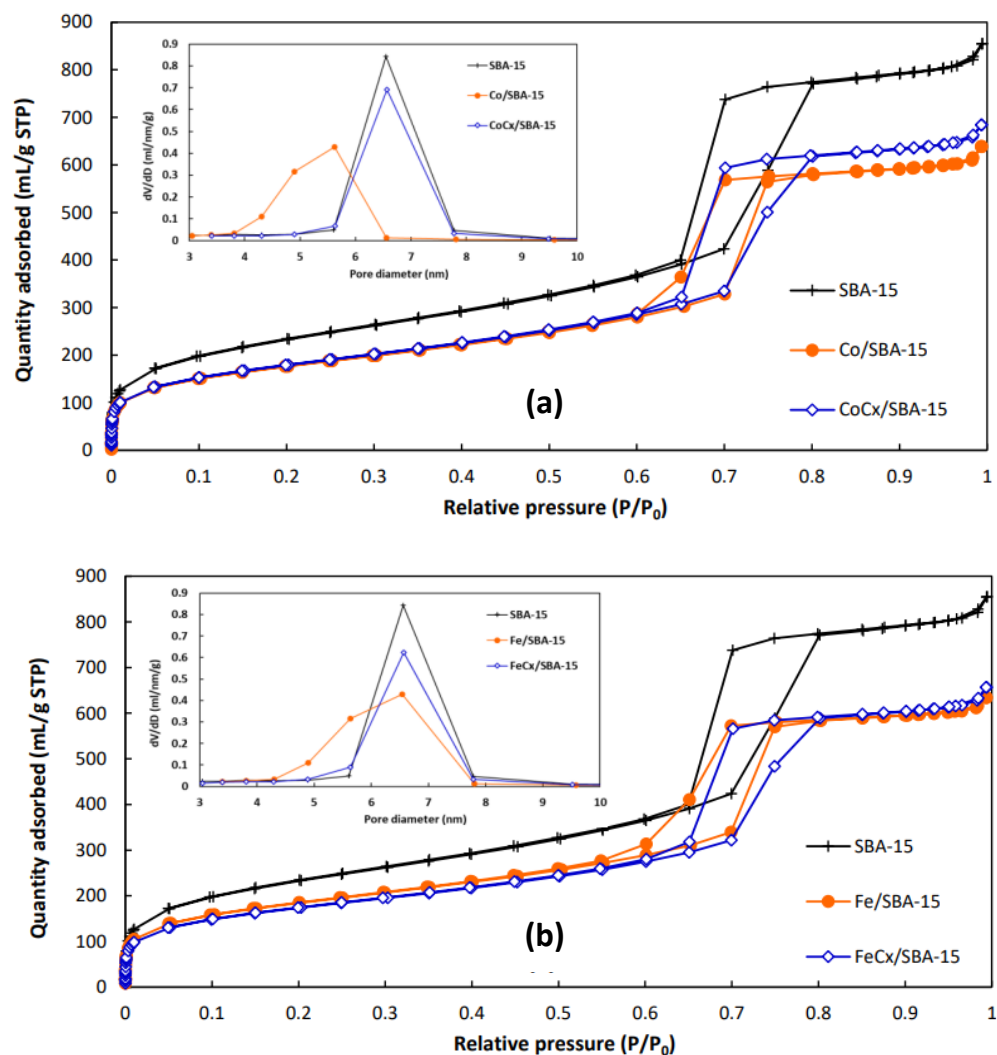

Figure 3. Adsorption–desorption isotherms of nitrogen and pore size distribution for fresh and used (**a**) cobalt-based and (**b**) iron-based catalysts.

Peaks belonging to CoO were also detected at 36° and 42.5° (PDF card no. 00-002-1217), which could form during the reduction of Co_3O_4 ($Co_3O_4 \rightarrow CoO \rightarrow Co$). The peak at 26.3° is a reflection of graphitic carbon (PDF card no. 41-1478), which could form due to coke deposition during the reaction. Another Co-based catalyst was used in the FT catalyst with a prior reduction step with hydrogen (U-Co/SBA-15-R), which did not show any obvious peaks for cobalt oxides, and very weak peaks for metallic Co were detected in this sample. The fresh cobalt carbide catalyst (Fresh CoCx/SBA-15) showed a weak peak for Co_2C 42.4°, 45.8°, and 56.6° (PDF card no. 65-1457), and small peaks for metallic cobalt were also observed for this catalyst.

The used cobalt carbide catalyst without reduction (U-CoCx/SBA-15-WR) showed very weak peaks belonging to metallic cobalt, as well as a peak ascribed to carbon. The U-CoCx-SBA-15 catalyst also did not show any significant peak except the main peak belonging to the amorphous SBA-15, and the detected peaks of metallic cobalt were very weak. During the reaction, cobalt oxide (Co_3O_4) is gradually reduced into CoO, and metallic

Co. Co_3O_4 can be active for the water gas shift reaction ($CO + H_2O \rightleftharpoons CO_2 + H$). Metallic cobalt is known as the main active phase for hydrocarbon production via FT reaction. Cobalt carbides are reported to positively affect the formation of olefins and oxygenates. Deposited graphitic carbon on the catalyst's surface leads to the catalyst deactivation, and it is crucial to avoid and reduce the carbon deposition to increase the catalyst's lifetime.
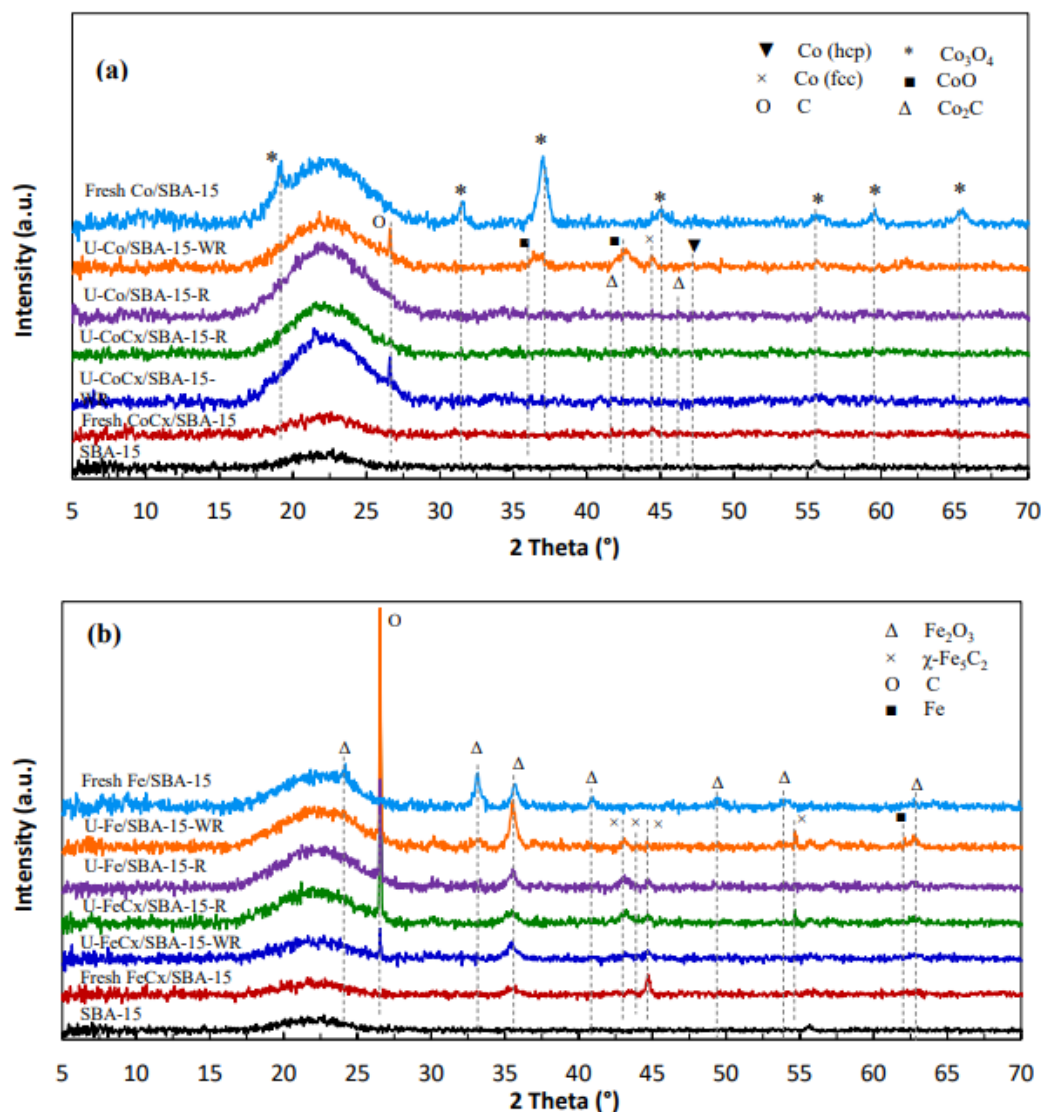

Figure 4. XRD patterns of (**a**) cobalt-based catalysts and (**b**) iron-based catalysts for fresh and used catalysts (U: used, R: with reduction step, WR: without reduction step).

Similar to the U-Co/SBA-15, the U-CoCx/SBA-15 catalyst also did not show any peak for carbon, which proved that coke deposition was impeded after reducing the catalysts with hydrogen prior to the FT reaction. The fresh Fe/SBA-15 catalyst showed peaks belonging to hematite Fe_2O_3 (PDF card no. 00-039-1346). After exposure to syngas during the reaction (U-Fe/SBA-15-WR), the peaks belonging to the iron carbide (χ-Fe_5C_2) were observed at 42.6°, 43.6°, 44.7°, and 54.9° (PDF card no. 00-051-0997) in these catalysts. The U-Fe/SBA-15-R catalyst, without the reduction step, did not show any peaks after the FT reaction except for the metallic state of Fe. On the contrary, the U-FeCx/SBA-15-R carbide catalyst had weak peaks for hematite Fe_2O_3 (PDF 00-039-1346) at 35.2° and for χ-Fe_5C_2 at 45°. The unreduced U-FeCx/SBA-15-WR carbide used catalyst showed very weak peaks corresponding to metallic iron, as well as a peak attributed to carbon, but had a stronger

peak for Fe_2O_3 at 35.3°. A freshly synthesized iron-based catalyst (Fresh FeCx/SBA-15) had a well-visible peak for χ-Fe_5C_2 at 44.9°.

Cobalt carbides are known as an active site for FT reaction, and iron oxides transform into iron carbides during the reaction. In the presence of hydrogen, the fresh iron catalyst undergoes reduction in both bulk and surface regions, resulting in the formation of Fe_3O_4 from the ferromagnetic (fm) and superparamagnetic (sp) structures of α-Fe_2O_3 (hematite) [26] (Figure 5). As reduction continues, Fe_3O_4 is converted to wüstite (FeO) and ultimately to metallic Fe (α-Fe). At temperatures above 200 °C in an inert atmosphere or at temperatures above 150 °C in a H_2-containing atmosphere, the disproportionation of FeO can occur kinetically [27]. Metallic iron is the primary active phase in Fe-based catalysts, and its transformation into iron carbides that can significantly affect the catalyst activity and product selectivity during the FT reaction. χ-Fe_5C_2 (Hägg carbide) is recognized as a highly active phase for the production of long-chain hydrocarbons, while FeO can act as an active phase for the water–gas shift reaction.
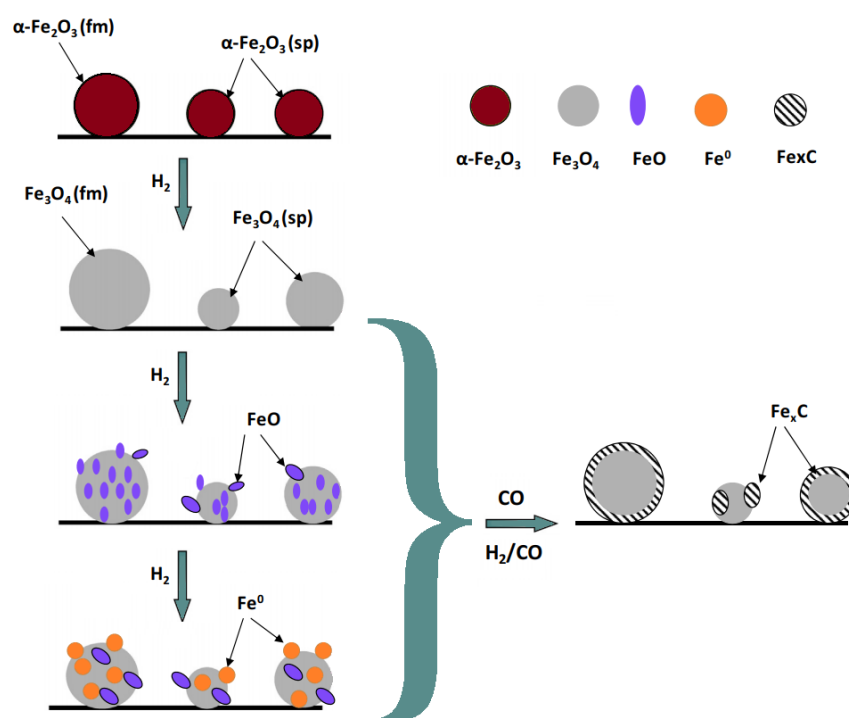
Figure 5. The behavior of an iron-based catalyst during reduction and carburization [26].

When the reduced catalyst is exposed to a syngas (CO + H_2) atmosphere, iron carbides (especially χ-Fe_5C_2) can be formed and act as the active sites for the FT reaction. During the reaction, various forms of iron oxides, including α-Fe, γ-Fe, Fe_3O_4, and FeO, may be present along with different types of iron carbides, including ε-Fe_2C, ε'-$Fe_{2.2}C$, χ-Fe_5C_2 (Hägg carbide), Fe_7C_3, and θ-Fe_3C [28–30]. All used iron-based catalysts showed a peak for graphitic carbon due to coke deposition during the FT reaction. Exposing the Fe/SBA-15 catalyst to hydrogen transformed Fe_2O_3 to Fe_3O_4, FeO, and finally metallic Fe, which then converted to iron carbide in the presence of syngas. A small peak of metallic iron was also detected in all used catalysts. The intensity of iron oxide peaks decreased, and the intensity of χ-Fe_5C_2 peaks slightly increased in the XRD pattern of the U-Fe/SBA-15-R catalyst. Due to the presence of more iron carbides, this catalyst is expected to have higher catalytic activity than the Fe/SBA-15-WR catalyst during the FT reaction. The fresh FeCx/SBA-15 catalyst showed a more intense peak of iron carbide, confirming the formation of χ-Fe_5C_2 during catalyst preparation. A small peak of Fe_2O_3 was detected, possibly due to the incomplete transformation of Fe_2O_3 to Fe_5C_2 during the catalyst preparation. After using this catalyst in the reaction, the intensity of the iron carbide peaks decreased, and an extra

peak of graphitic carbon was detected. Reducing the FeCx/SBA-15 with hydrogen could enhance the transformation of remaining iron oxides into iron carbide, leading to slightly higher activity during the reaction.

After conducting XRD analysis on cobalt and iron catalysts on SBA-15 with and without carbide phase for Fischer–Tropsch synthesis (FTS), various phases were identified. These phases have unique roles in the FTS reaction mechanism, ultimately affecting the catalyst's overall performance. For cobalt-based catalysts, CoO is crucial for activation, while Co_2C enhances the activity and selectivity towards olefins and oxygenates. Co_3O_4 phase acts as a promoter, providing active sites for the water–gas shift reaction. The crystal structure of metallic cobalt (hcp or fcc) also impacts its activity and selectivity, while carbon deposition can lead to deactivation.

Iron-based FTS catalysts also contain distinct phases that play vital roles in the reaction mechanism. Fe_2O_3 is responsible for activating iron-based catalysts, while χ-Fe_5C_2 promotes the formation of long-chain hydrocarbons, and FeO acts as a promoter for the water–gas shift reaction. The metallic Fe phase is considered the primary active phase, and its crystal structure significantly influences activity and selectivity toward different hydrocarbon products. However, carbon deposition on the catalyst surface can lead to deactivation, and it is crucial to consider this factor when evaluating catalyst performance.

3.1.4. TGA

Thermogravimetric curves of the analyzed fresh catalysts in an oxidative (O_2) and inert (N_2) atmosphere are shown in Figure 6a,b. The TGA curves indicate several areas of mass loss for all samples. In all cases, the first mass loss, which starts at 50 °C and ends at 100 °C, can be ascribed to the removal of adsorbed water (moisture). For non-carbide catalysts, this loss varied by about 2.5 wt.%, while for carbide catalysts, it was around 0.5–1.5 wt.%. It is also worth noting that carbon catalysts were more stable upon heating in both an inert and oxidative atmosphere. According to the differential thermogravimetric (DTG) curves of all fresh catalysts (Figure 4c,d), it can also be stated that the highest mass loss was at the beginning of the analysis in both inert and oxidative atmospheres and corresponds to the removal of water (moisture) from the samples. Subsequently, the mass change for all cases did not change significantly.

However, a small increase in mass is visible for carbide samples at a temperature of 200–500 °C. In the case of an oxidizing atmosphere, it can be ascribed to the formation of metal oxides and the subsequent burning of the samples. On the contrary, under an inert atmosphere, the decomposition of the samples should take place without a rise in weight, which could be due to the potential furnace leakage, leading to the reaction of residual air with the catalyst sample and the formation of oxides.

3.1.5. TGA Long-Term Analyses

Long-term TGA tests were conducted to determine the formation of the carbide phase on the catalyst surface and its mass percentage. Figures 7 and 8 show the experiment, which includes four temperature ramps up to 800 °C and a subsequent cooling step to 40 °C after each heating. For the cobalt-based catalyst, the first linear temperature increase occurred using air to remove volatile components, possible moisture from the catalyst surface, and chemically bound water inside the structure. At this step, the sample lost 7.1 wt.% of its mass, indicating that the mass of the catalyst became 316.1 mg. The second step involved the reduction of the catalyst to its metallic state in a hydrogen atmosphere, where oxygen atoms were removed as water (Equation (1)), resulting in a mass loss of about 2.3 wt.%. The third step used methane as a carbon source to form a carbide phase on the catalyst surface, with a weight gain of about 2.6 wt.%, indicating the formation of a carbide phase in the sample (Equation (2)). Thus, the sample mass remained approximately the same as after the first step. The final temperature ramp aimed to burn off all the carbon produced to determine its percentage, but it is likely that not all of the formed carbon was burned out, suggesting that the carbide phase formed not only on the surface but also within the

structure of the sample. This suggests the formation of a carbide phase not only on the surface but also in the structure of the sample, for which the temperature was insufficient for its removal.

$$Co_3O_4 + 4H_2 \rightarrow 3Co + 4H_2O \tag{1}$$

$$Co + 2CH_4 \rightarrow Co_2C + H_2 \tag{2}$$
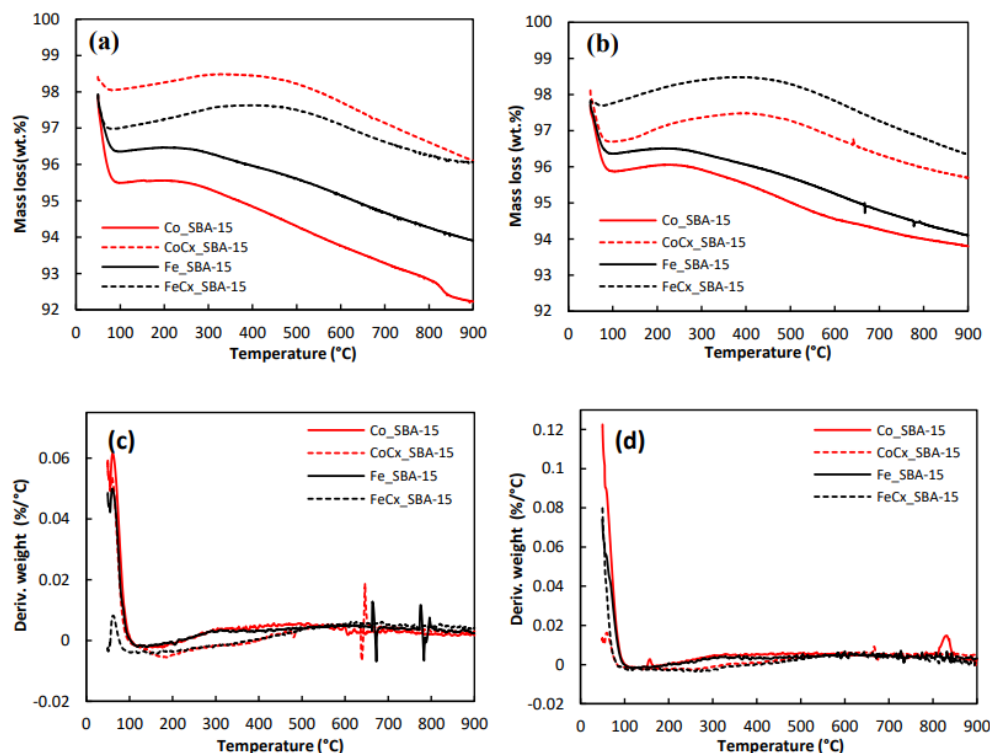
Figure 6. Thermogravimetric curves of fresh non-carbide catalysts (Co/SBA−15, Fe/SBA−15) and carbide catalysts (CoCx/SBA−15, FeCx/SBA−15) in nitrogen (**a**) and oxygen (**b**) atmosphere; Differential thermogravimetric (DTG) curves of fresh non-carbide catalysts (Co/SBA−15, Fe/SBA−15) and carbide catalysts (CoCx/SBA−15, FeCx/SBA−15) in (**c**) nitrogen and (**d**) oxygen atmosphere.

The experiment with the Fe/SBA-15 catalyst was carried out under the same conditions as the Co/SBA-15 catalyst (Figure 8). The first temperature ramp (step 1) followed the same course, with the removal of all moisture resulting in a weight loss of approximately 5.3 wt.%. During the second step (reduction with H_2), a further weight loss of around 1.9 wt.%. can be observed, corresponding to the conversion of the catalyst to the metallic state (Equation (3)). Subsequently, exposure of the reduced sample to methane resulted in an increase in weight of approximately 2.6 wt.%, indicating the formation of the carbide phase (Equation (4)). At the beginning of the fourth step in the air, a small increase in sample weight was observed, which could be due to the formation of oxides up to a temperature of about 400 °C. However, upon subsequent heating, the carbide phase began to decompose, resulting in a weight loss of 1.4 wt.%, indicating incomplete combustion of the bound carbon.
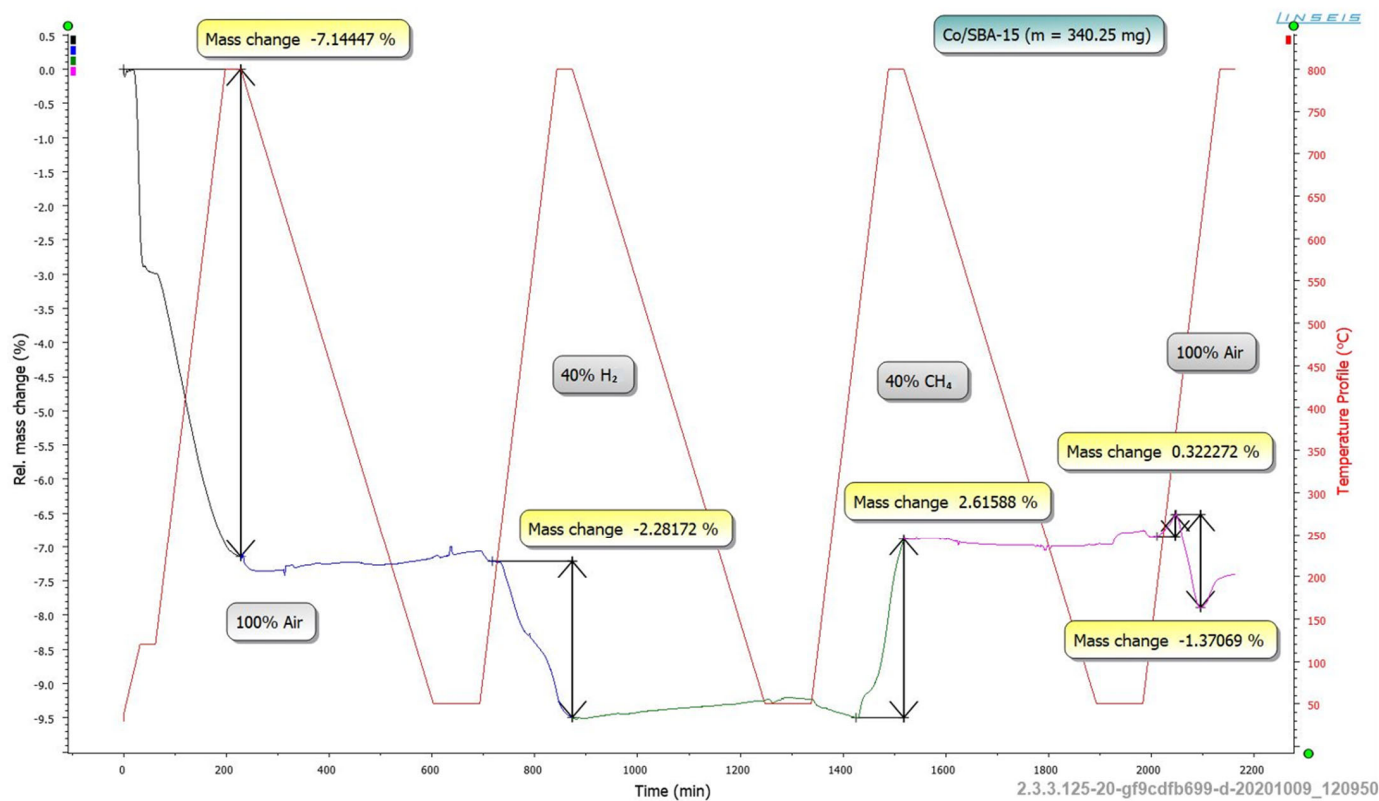
$$Fe_2O_3 + 3H_2 \rightarrow 2Fe + 3H_2O \tag{3}$$

$$Fe + 3CH_4 \rightarrow Fe_3C + 3H_2 \tag{4}$$

Figure 7. Long−term thermogravimetric analysis of Co/SBA−15 catalyst with four heating ramps temperature profile.
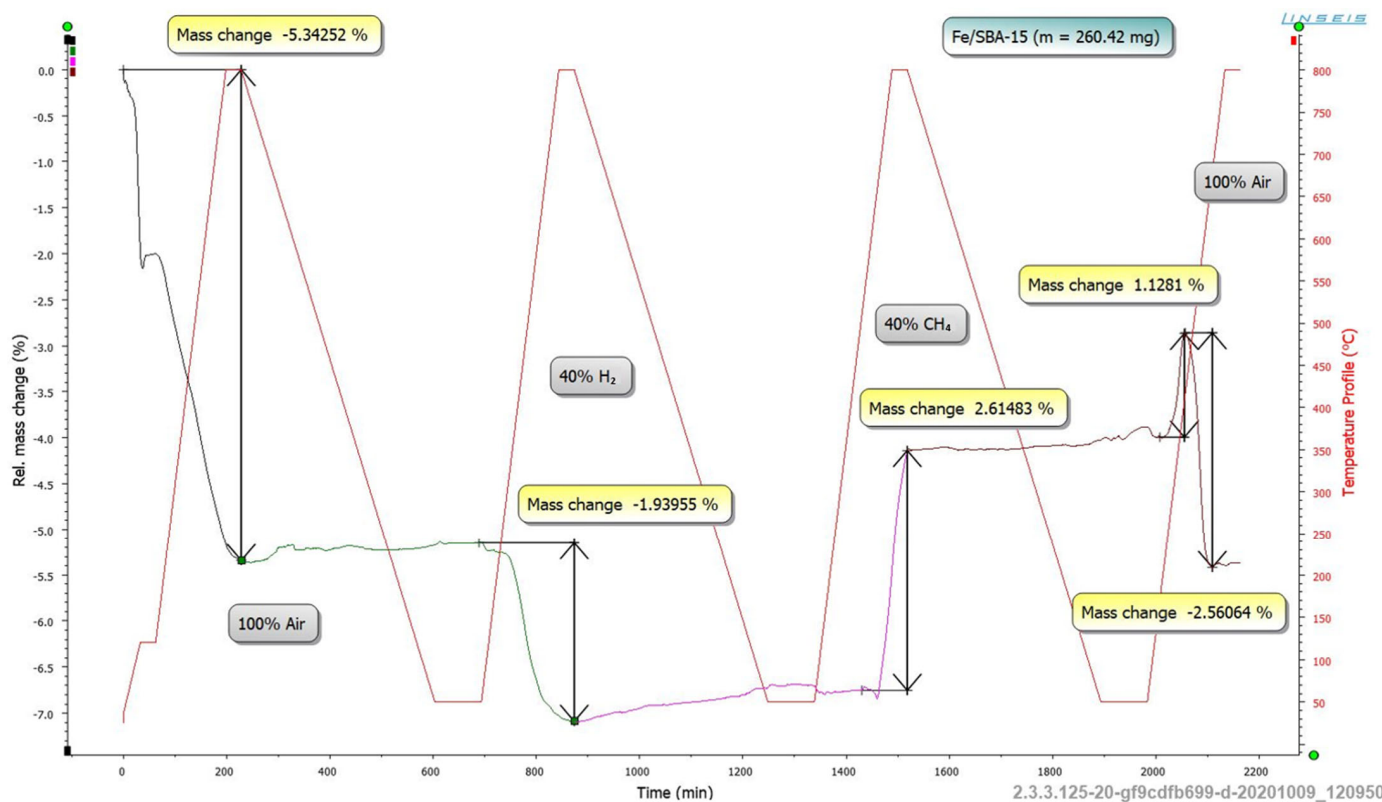

Figure 8. Long−term thermogravimetric analysis of Fe/SBA−15 catalyst with four heating ramps temperature profile.

The aim of this method was to determine whether the formation of a carbide phase is possible in these catalysts and in what percentage. Thus, based on a long thermogravimetric analysis of all samples, it can be concluded that the formation of the carbide phase occurs with approximately the same percentage content of about 2.6 wt.% for both Co/SBA-15 and Fe/SBA-15 catalysts.

3.1.6. ICP-OES

ICP-OES results (Table 2) showed that the main component of all catalysts was silicon oxide (about 84–92 wt.%), which forms the basis of the catalyst support. The metal content in all cases was in the expected range of 3.6–4.2 wt.%. However, as can be seen from the results, the carbon content was not determined by this method since its content was likely too low for detection.

Table 2. Co—cobalt, Fe—iron, C—carbon, and SiO_2—silicon oxide contents of fresh catalysts determined by the ICP-OES method.

Catalyst	Co (wt.%)	Fe (wt.%)	C (wt.%)	SiO_2 (wt.%)
Co/SBA-15	4.18	-	<0.06	86.6
Fe/SBA-15	-	3.79	<0.06	90.4
CoCx/SBA-15	3.97	-	<0.06	91.4
FeCx/SBA-15	-	3.64	<0.06	84.8

3.1.7. H_2-TPR

On the TPR curves shown in Figure 9, one can see the reduction of fresh catalysts and their pure SBA-15 support. The TPR profile recorded for the SBA-15 support had a wide range of reduction temperatures with only one weakly pronounced maximum observed above 350 °C. In the case of cobalt catalysts Co/SBA-15 and CoCx/SBA-15, it can be seen that for a carbide-free sample, reduction began with a two-step hydrogen consumption at temperatures between 200 °C and 350 °C. Following this, a second large peak was followed and completed below 550 °C, and hydrogen consumption ended below 800 °C. A similar situation was observed in the case of the cobalt carbide sample, with the only difference being that the first step occurred in one peak. The catalysts demonstrated high hydrogen consumption between 200 °C and 350 °C, which suggests a strong interaction between the active metal phase and the support compared to other catalysts.
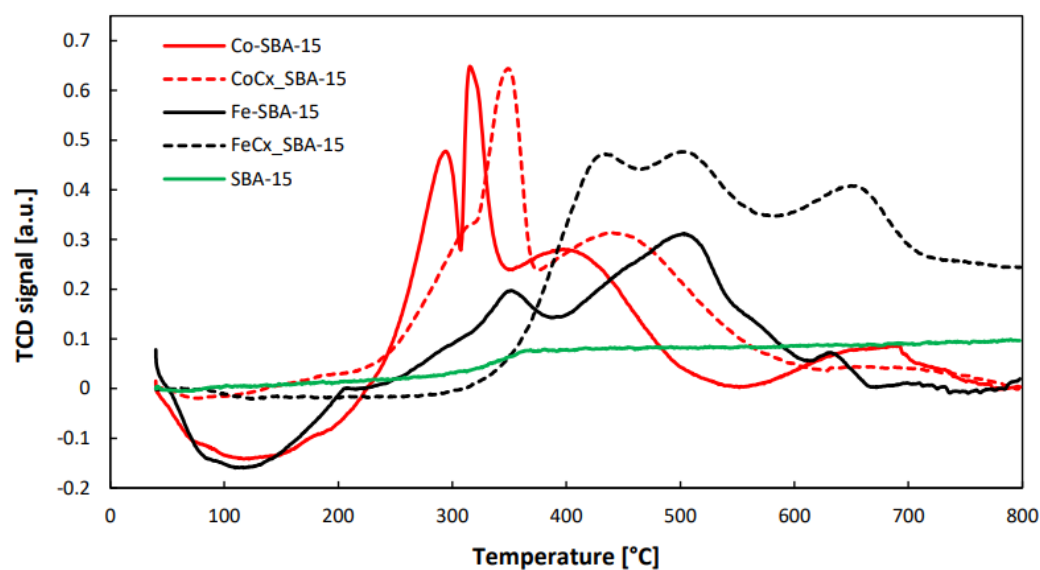

Figure 9. Temperature−programmed reduction profiles of all fresh catalysts and SBA−15 support.

In the case of iron catalysts Fe/SBA-15 and FeCx/SBA-15, the reduction occurred in three steps starting from 300 °C to 700 °C. However, as seen from the graph, the carbide sample had a higher hydrogen consumption, which could be due to a stronger metal-carbide interaction. Negative values of the TCD detector signal were observed in non-carbide samples, which could be due to the low content of metals in the catalysts, hindering their detection.

3.2. Catalytic Performance

The catalytic performance of the prepared cobalt- and iron-based catalysts was evaluated in an autoclave reactor, and the results are discussed in this section. The catalytic activity of catalysts, with and without reduction with hydrogen, was studied (Figure 10). For comparison, the catalytic performances of metal oxide catalysts (Co/SBA-15 and Fe/SBA-15) were also evaluated at the same reaction conditions with and without reduction with hydrogen. The non-reduced Co-SBA-15 catalyst did not show high activity, and the products were mainly in gaseous form. Reducing the catalyst with hydrogen resulted in the formation of Co^0 as the catalyst's active sites, and the catalyst's activity increased sharply, and CO conversion increased from about 16% to 73%, while the products were mainly heavier hydrocarbons in the liquid phase (73%). The CoCx/SBA-15 catalyst without reduction (CoCx/SBA-15-WR) showed better results than Co/SBA-15-WR. The CO conversion was 37%, with 68% selectivity to the products in the liquid phase. During the FT reaction, in the presence of syngas, the cobalt carbide could be decomposed to carbon and Co^0 (the active site for FT reaction) [31–33], resulting in a higher activity of the catalyst.
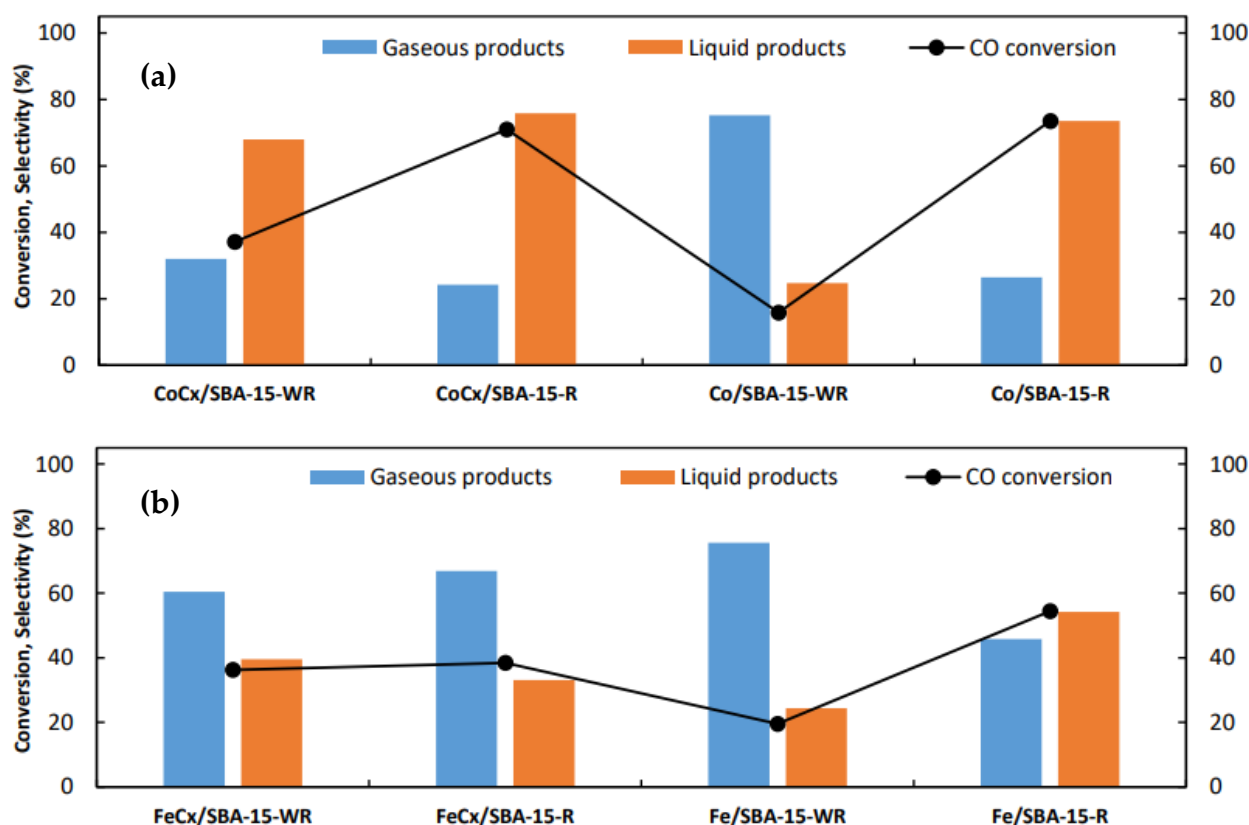

Figure 10. The distribution of gaseous and liquid products analyzed after 6 h of Fischer–Tropsch reaction at 230 °C. (**a**) Cobalt-based catalysts and (**b**) iron-based catalysts with and without reduction with hydrogen (R: with reduction step, WR: without reduction step).

The reduction of the CoCx/SBA-15 catalyst with hydrogen prior to the reaction (CoCx/SBA-15-R) resulted in a further increase in the catalyst's activity due to the higher transformation of cobalt species into the metallic form. At this condition, the CO conversion

increased to about 71% with 76% of liquid phase products. When cobalt carbides were exposed to hydrogen, they could be transformed into metallic cobalt with face-centered cubic (fcc) and hexagonal close-packed (hcp) structures. The fcc and hcp facets of cobalt with different bulk symmetries and structures have different intrinsic activity in the reaction [34]. Regarding the FT reaction, the hcp Co^0 nanoparticles are reported to be more active than Co^0 with fcc facet [34–36]. The reaction pathways over these two different cobalt structures are also different, and H-assisted CO dissociation mechanism (Equation (5)) is the main pathway over fcc cobalt facet, while the direct dissociation of CO (Equation (6)) is favored over hcp cobalt facet [34].

$$CO^* + H^* \rightarrow CHO^* \rightarrow CH^* + O^* \tag{5}$$

$$CO^* + H \rightarrow C^* + O^* + H^* \tag{6}$$
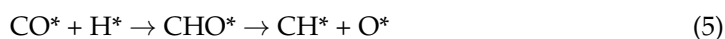
The analysis of gaseous products (Figure 11) showed that the products were mainly alkanes, with high selectivity to methane. By reducing the catalyst with hydrogen and forming metallic cobalt, it is expected to have more active sites for CO dissociation and the production of longer-chain hydrocarbons. The non-reduced CoCx/SBA-15-WR catalyst had a methane selectivity of 85% (Figure 11a), which reduced to 70% after catalyst reduction (CoCx/SBA-15-R), but at the same time, CO_2 formation increased over this catalyst. This observation may be attributed to the presence of cobalt carbide (Co_2C), which has (111) facets and is characterized by nanosphere-like particles. The formation of Co_2C can lead to reduced activity and higher selectivity towards methane [8,37,38].
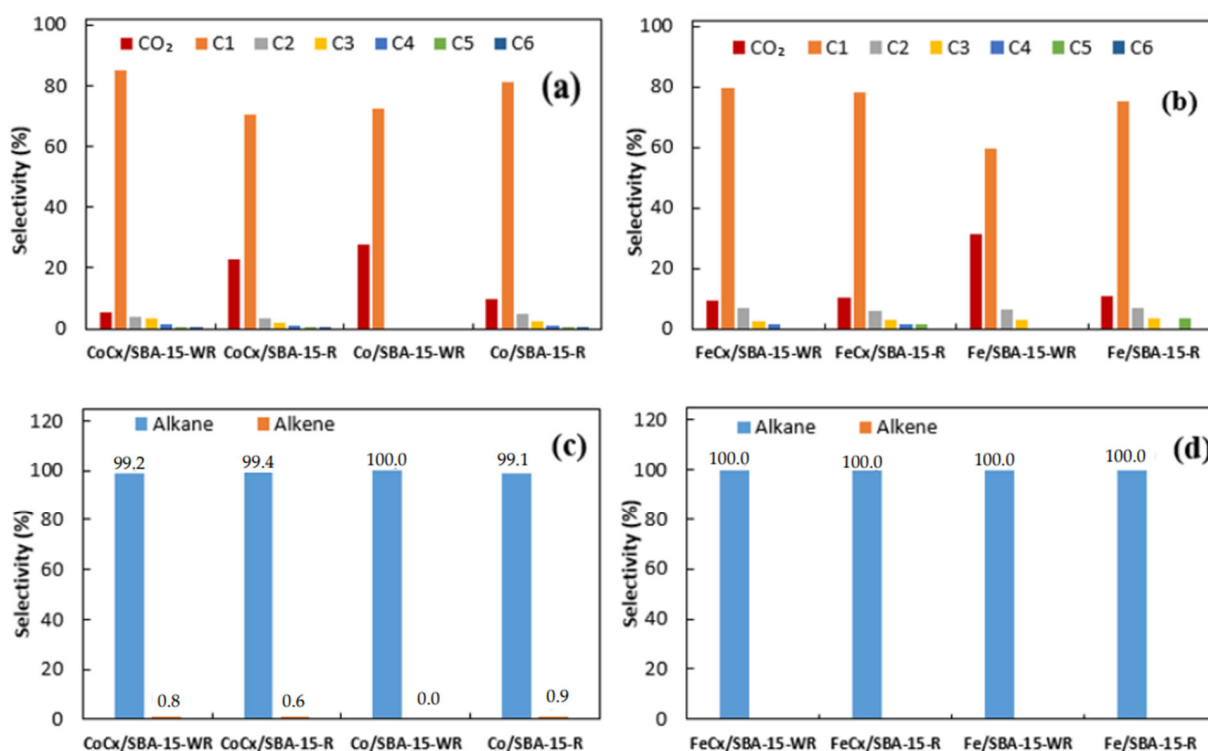
Figure 11. Gaseous product analysis in the FT reaction over (**a**) cobalt-based catalysts, (**b**) iron-based catalysts, (**c**) alkanes and alkene distribution over cobalt-based catalysts, and (**d**) alkanes and alkene distribution over iron-based catalysts (R: with reduction step, WR: without reduction step).

On the other hand, the Co/SBA-15-WR with the lowest catalytic activity and highest selectivity to gaseous phase products had the highest selectivity to CO_2 (27%), which then reduced sharply to 10% after reducing the Co/SBA-15 catalyst (Co/SBA-15-R). Methane was the only product observed during the reaction over Co/SBA-15-WR. The higher content of Co^0 could enhance the CO dissociation and the formation of more hydrocarbons

and less CO_2. However, this was not observed for the $CoCx/SBA-15$ catalysts, and after reduction with hydrogen, the formation of CO_2 increased. While the Co^0 active site is favored for CO dissociation and chain propagation, cobalt carbide (Co_2C (111)) is reported to be mainly active for the CO nondissociative activation and insertion mechanism [39,40]. The gaseous products were mainly alkanes, and the selectivity to alkenes was negligible (<1%) (Figure 11c).

Cobalt-based catalysts predominantly exhibit activity in their metallic state, whereas in the case of iron-based catalysts, reports have shown that iron oxides, iron carbides, and even metallic iron can act as active sites [26,41–43]. In this study, as shown in Figure 10b, the catalytic activity of $FeCx/SBA-15-WR$ (36%) was slightly lower than that of $FeCx/SBA-15-R$ (38%). The main product of the reaction over these two catalysts was gaseous products, mainly alkanes, with the highest selectivity to methane (Figure 11b,d). The hexagonal close-packed ε-carbide Fe_2C could be developed in small particles, while the χ-carbide Fe_5C_2 could be developed in larger particles. The catalytic activity depends on the carbide phase and its content. Several theoretical analysis characterizations have reported that the Hägg χ-Fe_5C_2 is the main active phase of the iron-based FT catalysts [44,45]. During the reduction of the carbide catalyst with hydrogen, the remaining oxide form of iron was reduced, which, in the presence of syngas, converted to iron carbides. Therefore, the activity increased slightly after the reduction of this catalyst.

Changing the reducing agent for Fe/SiO_2 catalyst could result in the formation of different carbide phases. Using hydrogen, carbon monoxide, and syngas as reducing agents leads to the formation of χ-Fe_5C_2 + ε-Fe_2C, χ-Fe_5C_2 + Fe_7C_3, and χ-Fe_5C_2 phases, respectively [46]. Chang et al. [46] observed that the presence of Fe_7C_3 can improve the catalyst activity, whereas the ε-Fe_2C phase can increase the selectivity towards C_{5+} products and decrease methane formation. The phase analysis of the iron catalyst supported on silica (Fe/SiO_2) was performed by Zhang et al. [47], and they found that the iron oxide mixtures (α-Fe_2O_3 (hematite) and maghemite (γ-Fe_2O_3)) are the main phases in the fresh supported catalyst, while after reduction of the catalyst with hydrogen, the main phases were FeO and iron (II) silicate (Fe_2SiO_4). The non-reduced catalyst ($Fe/SBA-15-WR$), which is mainly in the Fe_2O_3 form, did not show high activity, and the main product over this catalyst was alkanes (mainly methane) (Figure 11b,d).

The reduction of the $Fe/SBA-15$ catalyst with hydrogen could result in the formation of more reduced iron, which can easily convert to iron carbides (χ-Fe_5C_2 + ε-Fe_2C) with high activity in the FT reaction. The main product over this catalyst was the products in the liquid phase, and the selectivity to heavier hydrocarbons increased slightly over this catalyst.

The evaluation of the liquid phase products for both cobalt- and iron-based catalysts (with and without the reduction step) showed that longer-chain hydrocarbons formed over the $CoCx/SBA-15$ catalysts (Figure 12). The decomposition of cobalt carbides and formation of more hcp Co^0 with higher selectivity to long-chain hydrocarbons could be the reason for these results. The non-reduced $Co/SBA-15-WR$ with the lowest conversion showed selectivity to hydrocarbons up to C10. By reducing the catalyst with hydrogen and forming cobalt active sites, longer-chain hydrocarbons were formed during the FT reaction. As expected, the iron-based catalysts resulted in the formation of lighter hydrocarbons up to C_{18} with the highest selectivity to C_6-C_7 hydrocarbons.

The iron carbide catalyst ($FeCx/SBA-15-WR$) produced hydrocarbons in the range of C_4-C_{11} and reducing the catalyst with hydrogen prior to the reaction resulted in the formation of slightly heavier hydrocarbons (up to C_{16}). As mentioned earlier, during the reduction of the catalyst with hydrogen, some iron oxide (Fe_2O_3) that was not converted to iron carbide during the preparation of the carbide catalyst could be converted to the metallic form of iron, which then transformed into iron carbides in the presence of syngas. The $Fe/SBA-15-WR$, with a mixture of iron oxides as the main phase and low CO conversion, led to the formation of light hydrocarbons. Reducing the $Fe/SBA-15$ catalyst with hydrogen resulted in the formation of iron carbides (mainly χ-Fe_5C_2 + ε-Fe_2C) with higher catalytic activity and selectivity to C_{5+} hydrocarbons. Similar to the gaseous phase products, in this

research, the main products in the liquid phase were alkanes over both cobalt- and iron-based catalysts (Figure 12c,d). A study by Yin et al. [48] examined the effect of Fe_2O_3, Fe_3O_4, and Fe_5C_2 phases on Fe/SiO_2 catalysts for FTS. They found that the presence of Fe_5C_2 promoted the formation of higher molecular weight hydrocarbons, which is consistent with our findings for iron carbide catalysts. However, they did not observe a significant difference in catalytic activity between the reduced and non-reduced catalysts, which differs from our results for the iron carbide catalysts.
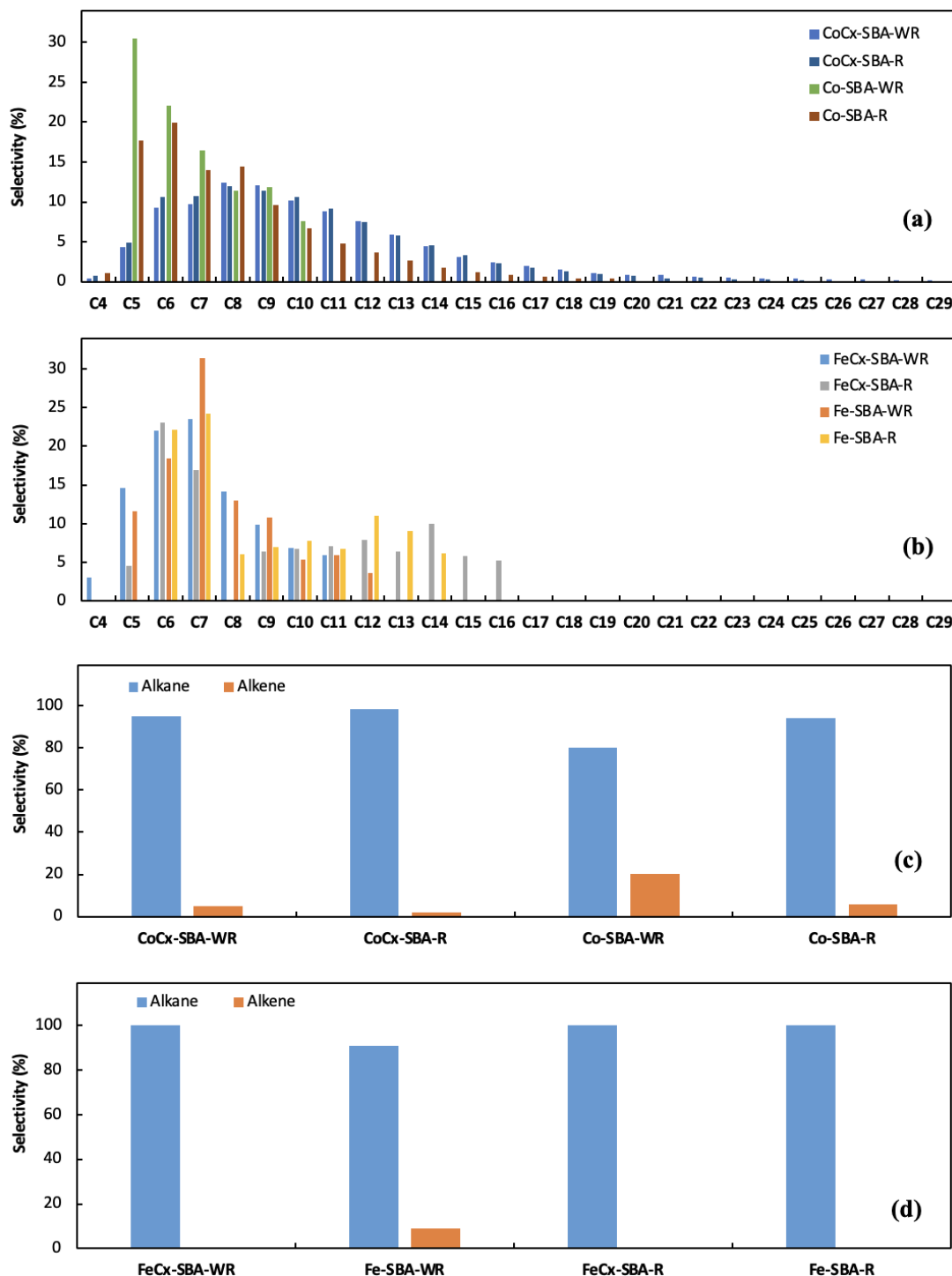
Figure 12. Liquid product analysis in the FT reaction over (**a**) cobalt-based catalysts, (**b**) iron-based catalysts, (**c**) alkanes and alkene distribution over cobalt-based catalysts, and (**d**) alkanes and alkene distribution over iron-based catalysts (R: with reduction step, WR: without reduction step).

4. Conclusions

The catalytic efficacy of the cobalt-based and iron-based catalysts, with and without the carbide phase, was assessed in a Fischer–Tropsch synthesis reaction using an autoclave reactor. The catalytic potential of both cobalt and iron catalysts was investigated with and without reduction with hydrogen. The results of this study highlight the important role of the carbide phase in promoting the synthesis of higher-value hydrocarbons from syngas. The non-reduced Co-SBA-15 catalyst did not show high catalytic activity (16%), while reducing the catalyst and formation of metallic cobalt resulted in an increase in CO conversion to 73%, and at the same time, selectivity to C_{5+} increased to 73%. Reduction of the CoCx/SBA-15 catalyst with hydrogen prior to the reaction (CoCx/SBA-15-R) led to a higher catalytic activity (71%) than the non-reduced CoCx/SBA-15 catalyst (37%) due to the higher transformation of cobalt species into the metallic form (mainly hcp Co^0 nanoparticles) in the presence of hydrogen during the reduction step. The formation of C_{5+} also increased from 68% to 76%. Reducing the catalyst with hydrogen and forming metallic cobalt led to the formation of more active sites for CO dissociation and the production of longer-chain hydrocarbons.

Notably, iron carbide catalysts showed promising catalytic activity and selectivity towards C_{5+} hydrocarbons, with the FeCx/SBA-15-WR catalyst producing hydrocarbons in the range of C_4-C_{11} and slightly heavier hydrocarbons (up to C_{16}) upon reduction with hydrogen prior to the reaction. The presence of iron carbides, iron oxides, and metallic iron during the reaction was found to have a notable influence on the catalytic performance. Interestingly, the presence of iron oxide in the Fe/SBA-15-WR catalyst led to the formation of lighter hydrocarbons with low CO conversion, underscoring the importance of the carbide phase for selective hydrocarbon synthesis. Overall, the findings of this study provide valuable insights into the design and optimization of carbide catalysts for the efficient conversion of syngas to high-value hydrocarbons, with potential implications for the development of sustainable and economically viable energy technologies.

Author Contributions: Methodology, N.S. and Z.G.; Validation, Z.G., Z.T. and J.Š.; Formal analysis, N.S. and Z.G.; Investigation, N.S. and Z.G., I.H., Z.T. and J.Š.; Data curation, N.S. and Z.G.; Writing—original draft, N.S. and Z.G.; Writing—review & editing, N.S., Z.G., I.H., Z.T. and J.Š.; Visualization, N.S. and Z.G. All authors have read and agreed to the published version of the manuscript.

Data Availability Statement: The data that support the findings of this study are available from the corresponding author upon reasonable request.

Conflicts of Interest: The authors declare no conflict of interest.

References

1. Saheli, S.; Rezvani, A.R.; Izadpanah, A.; Dusek, M.; Eigner, V. Design novel inorganic precursors for producing clean fuels by using Fischer-Tropsch synthesis. *J. Saudi Chem. Soc.* **2019**, *23*, 1070–1079. [CrossRef]
2. Li, W.-Z.; Liu, J.-X.; Gu, J.; Zhou, W.; Yao, S.-Y.; Si, R.; Guo, Y.; Su, H.-Y.; Yan, C.-H.; Li, W.-X.; et al. Chemical Insights into the Design and Development of Face-Centered Cubic Ruthenium Catalysts for Fischer–Tropsch Synthesis. *J. Am. Chem. Soc.* **2017**, *139*, 2267–2276. [CrossRef]
3. Sirikulbodee, P.; Ratana, T.; Sornchamni, T.; Phongaksorn, M.; Tungkamani, S. Catalytic performance of Iron-based catalyst in Fischer–Tropsch synthesis using CO_2 containing syngas. *Energy Procedia* **2017**, *138*, 998–1003. [CrossRef]
4. Gholami, Z.; Tišler, Z.; Rubáš, V. Recent advances in Fischer-Tropsch synthesis using cobalt-based catalysts: A review on supports, promoters, and reactors. *Catal. Rev.* **2020**, *63*, 512–595. [CrossRef]

5. Lin, T.; Gong, K.; Wang, C.; An, Y.; Wang, X.; Qi, X.; Li, S.; Lu, Y.; Zhong, L.; Sun, Y. Fischer–Tropsch Synthesis to Olefins: Catalytic Performance and Structure Evolution of Co_2C-Based Catalysts under a CO_2 Environment. *ACS Catal.* **2019**, *9*, 9554–9567. [CrossRef]

6. Xiang, Y.; Kruse, N. Tuning the catalytic CO hydrogenation to straight- and long-chain aldehydes/alcohols and olefins/paraffins. *Nat. Commun.* **2016**, *7*, 13058. [CrossRef] [PubMed]

7. Yang, R.; Xia, Z.; Zhao, Z.; Sun, F.; Du, X.; Yu, H.; Gu, S.; Zhong, L.; Zhao, J.; Ding, Y.; et al. Characterization of CoMn catalyst by in situ X-ray absorption spectroscopy and wavelet analysis for Fischer–Tropsch to olefins reaction. *J. Energy Chem.* **2019**, *32*, 118–123. [CrossRef]

8. Zhong, L.; Yu, F.; An, Y.; Zhao, Y.; Sun, Y.; Li, Z.; Lin, T.; Lin, Y.; Qi, X.; Dai, Y.; et al. Cobalt carbide nanoprisms for direct production of lower olefins from syngas. *Nature* **2016**, *538*, 84–87. [CrossRef]

9. Gnanamani, M.K.; Jacobs, G.; Graham, U.M.; Ribeiro, M.C.; Noronha, F.B.; Shafer, W.D.; Davis, B.H. Influence of carbide formation on oxygenates selectivity during Fischer-Tropsch synthesis over Ce-containing Co catalysts. *Catal. Today* **2016**, *261*, 40–47. [CrossRef]

10. Chen, P.-P.; Liu, J.-X.; Li, W.-X. Carbon Monoxide Activation on Cobalt Carbide for Fischer–Tropsch Synthesis from First-Principles Theory. *ACS Catal.* **2019**, *9*, 8093–8103. [CrossRef]

11. Lebarbier, V.M.; Mei, D.; Kim, D.H.; Andersen, A.; Male, J.L.; Holladay, J.E.; Rousseau, R.; Wang, Y. Effects of La_2O_3 on the Mixed Higher Alcohols Synthesis from Syngas over Co Catalysts: A Combined Theoretical and Experimental Study. *J. Phys. Chem. C* **2011**, *115*, 17440–17451. [CrossRef]

12. Pei, Y.-P.; Liu, J.-X.; Zhao, Y.-H.; Ding, Y.-J.; Liu, T.; Dong, W.-D.; Zhu, H.-J.; Su, H.-Y.; Yan, L.; Li, J.-L.; et al. High Alcohols Synthesis via Fischer–Tropsch Reaction at Cobalt Metal/Carbide Interface. *ACS Catal.* **2015**, *5*, 3620–3624. [CrossRef]

13. Zhang, S.; Liu, X.; Shao, Z.; Wang, H.; Sun, Y. Direct CO2 hydrogenation to ethanol over supported Co_2C catalysts: Studies on support effects and mechanism. *J. Catal.* **2020**, *382*, 86–96. [CrossRef]

14. Dai, Y.; Zhao, Y.; Lin, T.; Li, S.; Yu, F.; An, Y.; Wang, X.; Xiao, K.; Sun, F.; Jiang, Z.; et al. Particle Size Effects of Cobalt Carbide for Fischer–Tropsch to Olefins. *ACS Catal.* **2018**, *9*, 798–809. [CrossRef]

15. Zhao, D.; Feng, J.; Huo, Q.; Melosh, N.; Fredrickson, G.H.; Chmelka, B.F.; Stucky, G.D. Triblock Copolymer Syntheses of Mesoporous Silica with Periodic 50 to 300 Angstrom Pores. *Science* **1998**, *279*, 548–552. [CrossRef] [PubMed]

16. Dancuart, L.P.; de Haan, R.; de Klerk, A. Processing of Primary Fischer-Tropsch Products. In *Studies in Surface Science and Catalysis*; Elsevier: Amsterdam, The Netherlands, 2004; Volume 152, Chapter 6, pp. 482–532. [CrossRef]

17. Trofimova, E.Y.; Kurdyukov, D.A.; Kukushkina, Y.A.; Yagovkina, M.A.; Golubev, V.G. Synthesis of monodispersed mesoporous spheres of submicron size amorphous silica. *Glass Phys. Chem.* **2011**, *37*, 378–384. [CrossRef]

18. Zhao, D.; Sun, J.; Li, Q.; Stucky, G.D. Morphological Control of Highly Ordered Mesoporous Silica SBA-15. *Chem. Mater.* **2000**, *12*, 275–279. [CrossRef]

19. Lu, Q.; Wang, Z.; Li, J.; Wang, P.; Ye, X. Structure and Photoluminescent Properties of ZnO Encapsulated in Mesoporous Silica SBA-15 Fabricated by Two-Solvent Strategy. *Nanoscale Res. Lett.* **2009**, *4*, 646–654. [CrossRef]

20. Zukal, A.; Siklová, H.; Cejka, J. Grafting of Alumina on SBA-15: Effect of Surface Roughness. *Langmuir* **2008**, *24*, 9837–9842. [CrossRef]

21. Gholami, Z.; Tišler, Z.; Svobodová, E.; Hradecká, I.; Sharkov, N.; Gholami, F. Catalytic Performance of Alumina-Supported Cobalt Carbide Catalysts for Low-Temperature Fischer–Tropsch Synthesis. *Catalysts* **2022**, *12*, 1222. [CrossRef]

22. Sing, K. Reporting physisorption data for gas/solid systems with special reference to the determination of surface area and porosity (Provisional). *Pure Appl. Chem.* **1982**, *54*, 2201–2218. [CrossRef]

23. Thommes, M.; Kaneko, K.; Neimark, A.V.; Olivier, J.P.; Rodriguez-Reinoso, F.; Rouquerol, J.; Sing, K.S. Physisorption of gases, with special reference to the evaluation of surface area and pore size distribution (IUPAC Technical Report). *Pure Appl. Chem.* **2015**, *87*, 1051–1069. [CrossRef]

24. Fan, X.; Li, J.; Zhao, Z.; Wei, Y.; Liu, J.; Duan, A.; Jiang, G. Dehydrogenation of propane over PtSn/SBA-15 catalysts: Effect of the amount of metal loading and state. *RSC Adv.* **2015**, *5*, 28305–28315. [CrossRef]

25. Yao, Q.; Lu, Z.-H.; Yang, K.; Chen, X.; Zhu, M. Ruthenium nanoparticles confined in SBA-15 as highly efficient catalyst for hydrolytic dehydrogenation of ammonia borane and hydrazine borane. *Sci. Rep.* **2015**, *5*, 15186. [CrossRef]

26. Ding, M.; Yang, Y.; Wu, B.; Li, Y.; Wang, T.; Ma, L. Study on reduction and carburization behaviors of iron phases for iron-based Fischer–Tropsch synthesis catalyst. *Appl. Energy* **2015**, *160*, 982–989. [CrossRef]

27. Mogorosi, R.P.; Fischer, N.; Claeys, M.; van Steen, E. Strong-metal–support interaction by molecular design: Fe–silicate interactions in Fischer–Tropsch catalysts. *J. Catal.* **2012**, *289*, 140–150. [CrossRef]

28. Abelló, S.; Montané, D. Exploring Iron-based Multifunctional Catalysts for Fischer–Tropsch Synthesis: A Review. *ChemSusChem* **2011**, *4*, 1538–1556. [CrossRef] [PubMed]

29. Ribeiro, M.C.; Jacobs, G.; Davis, B.H.; Cronauer, D.C.; Kropf, A.J.; Marshall, C.L. Fischer−Tropsch Synthesis: An In-Situ TPR-EXAFS/XANES Investigation of the Influence of Group I Alkali Promoters on the Local Atomic and Electronic Structure of Carburized Iron/Silica Catalysts. *J. Phys. Chem. C* **2010**, *114*, 7895–7903. [CrossRef]

30. Bian, G.; Oonuki, A.; Koizumi, N.; Nomoto, H.; Yamada, M. Studies with a precipitated iron Fischer-Tropsch catalyst reduced by H_2 or CO. *J. Mol. Catal. A Chem.* **2002**, *186*, 203–213. [CrossRef]

31. Mohandas, J.C.; Gnanamani, M.K.; Jacobs, G.; Ma, W.; Ji, Y.; Khalid, S.; Davis, B.H. Fischer–Tropsch Synthesis: Characterization and Reaction Testing of Cobalt Carbide. *ACS Catal.* **2011**, *1*, 1581–1588. [CrossRef]

32. Moya-Cancino, J.G.; Honkanen, A.-P.; van der Eerden, A.M.J.; Oord, R.; Monai, M.; ten Have, I.; Sahle, C.J.; Meirer, F.; Weckhuysen, B.M.; de Groot, F.M.F.; et al. In Situ X-ray Raman Scattering Spectroscopy of the Formation of Cobalt Carbides in a Co/TiO2 Fischer–Tropsch Synthesis Catalyst. *ACS Catal.* **2021**, *11*, 809–819. [CrossRef]

33. Lin, Q.; Liu, B.; Jiang, F.; Fang, X.; Xu, Y.; Liu, X. Assessing the formation of cobalt carbide and its catalytic performance under realistic reaction conditions and tuning product selectivity in a cobalt-based FTS reaction. *Catal. Sci. Technol.* **2019**, *9*, 3238–3258. [CrossRef]

34. Liu, J.-X.; Su, H.-Y.; Sun, D.-P.; Zhang, B.-Y.; Li, W.-X. Crystallographic Dependence of CO Activation on Cobalt Catalysts: HCP versus FCC. *J. Am. Chem. Soc.* **2013**, *135*, 16284–16287. [CrossRef] [PubMed]

35. Ten Have, I.C.; Weckhuysen, B.M. The active phase in cobalt-based Fischer-Tropsch synthesis. *Chem Catal.* **2021**, *1*, 339–363. [CrossRef]

36. Lyu, S.; Wang, L.; Zhang, J.; Liu, C.; Sun, J.; Peng, B.; Wang, Y.; Rappé, K.G.; Zhang, Y.; Li, J.; et al. Role of Active Phase in Fischer–Tropsch Synthesis: Experimental Evidence of CO Activation over Single-Phase Cobalt Catalysts. *ACS Catal.* **2018**, *8*, 7787–7798. [CrossRef]

37. Xiao, Y.; Sun, P.; Cao, M. Core–Shell Bimetallic Carbide Nanoparticles Confined in a Three-Dimensional N-Doped Carbon Conductive Network for Efficient Lithium Storage. *ACS Nano* **2014**, *8*, 7846–7857. [CrossRef]

38. Lin, T.; Yu, F.; An, Y.; Qin, T.; Li, L.; Gong, K.; Zhong, L.; Sun, Y. Cobalt Carbide Nanocatalysts for Efficient Syngas Conversion to Value-Added Chemicals with High Selectivity. *Acc. Chem. Res.* **2021**, *54*, 1961–1971. [CrossRef]

39. An, Y.; Lin, T.; Yu, F.; Wang, X.; Lu, Y.; Zhong, L.; Wang, H.; Sun, Y. Effect of Reaction Pressures on Structure–Performance of Co2C-Based Catalyst for Syngas Conversion. *Ind. Eng. Chem. Res.* **2018**, *57*, 15647–15653. [CrossRef]

40. Choi, Y.I.; Yang, J.H.; Park, S.J.; Sohn, Y. Energy Storage and CO_2 Reduction Performances of Co/Co_2C/C Prepared by an Anaerobic Ethanol Oxidation Reaction Using Sacrificial SnO_2. *Catalysts* **2020**, *10*, 1116. [CrossRef]

41. Dry, M.E. Fischer-Tropsch synthesis over iron catalysts. *Catal. Lett.* **1990**, *7*, 241–251. [CrossRef]

42. Davis, B.H. Fischer−Tropsch Synthesis: Comparison of Performances of Iron and Cobalt Catalysts. *Ind. Eng. Chem. Res.* **2007**, *46*, 8938–8945. [CrossRef]

43. Khodakov, A.Y.; Chu, W.; Fongarland, P. Advances in the Development of Novel Cobalt Fischer−Tropsch Catalysts for Synthesis of Long-Chain Hydrocarbons and Clean Fuels. *Chem. Rev.* **2007**, *107*, 1692–1744. [CrossRef] [PubMed]

44. Wang, D.; Chen, B.; Duan, X.; Chen, D.; Zhou, X. Iron-based Fischer–Tropsch synthesis of lower olefins: The nature of χ-Fe_5C_2 catalyst and why and how to introduce promoters. *J. Energy Chem.* **2016**, *25*, 911–916. [CrossRef]

45. Chen, B.; Wang, D.; Duan, X.; Liu, W.; Li, Y.; Qian, G.; Yuan, W.; Holmen, A.; Zhou, X.; Chen, D. Charge-Tuned CO Activation over a χ-Fe_5C_2 Fischer–Tropsch Catalyst. *ACS Catal.* **2018**, *8*, 2709–2714. [CrossRef]

46. Chang, Q.; Zhang, C.; Liu, C.; Wei, Y.; Cheruvathur, A.V.; Dugulan, A.I.; Niemantsverdriet, J.W.; Liu, X.; He, Y.; Qing, M.; et al. Relationship between Iron Carbide Phases (ε-Fe_2C, Fe_7C_3, and χ-Fe_5C_2) and Catalytic Performances of Fe/SiO_2 Fischer–Tropsch Catalysts. *ACS Catal.* **2018**, *8*, 3304–3316. [CrossRef]

47. Zhang, C.-H.; Wan, H.-J.; Yang, Y.; Xiang, H.-W.; Li, Y.-W. Study on the iron–silica interaction of a co-precipitated Fe/SiO_2 Fischer–Tropsch synthesis catalyst. *Catal. Commun.* **2006**, *7*, 733–738. [CrossRef]

48. Yin, J.; He, Y.; Liu, X.; Zhou, X.; Huo, C.F.; Guo, W.; Peng, Q.; Yang, Y.; Jiao, H.; Li, Y.W.; et al. Visiting CH_4 formation and C_1 + C_1 couplings to tune CH_4 selectivity on Fe surfaces. *J. Catal.* **2019**, *372*, 217–225. [CrossRef]